Wind and Structures, *Vol. 30, No. 1 (2020) 85-97*
DOI: https://doi.org/10.12989/was.2020.30.1.085

Buffeting response of a free-standing bridge pylon in a trumpet-shaped mountain pass

Jiawu Li[1,2a], Zhengfeng Shen[*1,2], Song Xing[1,2] and Guangzhong Gao[1,2]

[1] *School of Highway, Chang'an University, Xi'an, 710064, Shaanxi, China*
[2] *Key Laboratory for Bridge and Tunnel of Shaanxi Province, Chang'an University, Xi'an, 710064, Shaanxi, China*

(Received August 18, 2019, Revised October 31, 2019, Accepted November 22, 2019)

Abstract. The accurate estimation of the buffeting response of a bridge pylon is related to the quality of the bridge construction. To evaluate the influence of wind field characteristics on the buffeting response of a pylon in a trumpet-shaped mountain pass, this paper deduced a multimodal coupled buffeting frequency domain calculation method for a variable-section bridge tower under the twisted wind profile condition based on quasi-steady theory. Through the long-term measurement of the wind field of the trumpet-shaped mountain pass, the wind characteristics were studied systematically. The effects of the wind characteristics, wind yaw angles, mean wind speeds, and wind profiles on the buffeting response were discussed. The results show that the mean wind characteristics are affected by the terrain and that the wind profile is severely twisted. The optimal fit distribution of the monthly and annual maximum wind speeds is the log-logistic distribution, and the generalized extreme value I distribution may underestimate the return wind speed. The design wind characteristics will overestimate the buffeting response of the pylon. The buffeting response of the pylon is obviously affected by the wind yaw angle and mean wind speed. To accurately estimate the buffeting response of the pylon in an actual construction, it is necessary to consider the twisted effect of the wind profile.

Keywords: bridge pylon; trumpet-shaped mountain pass; twisted wind profile; wind spectrum; coherence function; buffeting response

1. Introduction

The buffeting response of a flexible structure is affected by the wind characteristics (Hui *et al.* 2009). However, the wind characteristics are significantly different between a homogeneous terrain and a complex terrain. Hence, the wind characteristics of the wind-resistant design specification, which is based on the homogeneous terrain, cannot be used directly for the buffeting response calculation of a bridge in a complex terrain (Hu *et al*. 2018). In recent years, there have been numerous studies in the literature performed on a long-term-monitored wind field that analyzed the influence of the wind characteristics on the buffeting response (Hu *et al*. 2013, Wang *et al*. 2013, Tao *et al*. 2016). Furthermore, the buffeting response measured by wind and structural health monitoring (WASHM) systems has been compared with the calculated buffeting response, which provided an opportunity to verify the classical theory of buffeting (Cheynet *et al*. 2016, Fenerci and Øiseth 2017, 2018). Unfortunately, the study of the wind characteristics of a complex terrain has mainly focused on the gorge terrain, mountainous terrain or fjord, and little attention has been paid to the mountain pass. In addition, the study of the buffeting response based on measured wind characteristics mainly focused on the main beam of a bridge. More specifically, there have been few studies on the wind-induced vibration of a bridge pylon under the measured wind characteristics. However, the pylons in complex mountain areas are very high, e.g., the Pingtang Bridge (332 m) and Millau Viaduct (343 m). Therefore, a pylon is sensitive to wind loads.

Obviously, the wind load has little influence on the vibration response of a pylon under the influence of the gravity stiffness of the cable after a bridge is completed. However, the free-standing pylons are sensitive to the wind loads under construction conditions (Fujino *et al*. 2012). Ricciardelli (1996) conducted a wind tunnel test on a fixed sectional model and proposed a semiempirical method for calculating the wind-induced response. Larose *et al*. (1998) measured the wind-induced response of a free-standing bridge pylon by accelerometers. The vortex-induced vibrations of the bridge pylon were investigated by the wind tunnel test and full-scale measurement (Marra *et al*. 2017). Guo *et al*. (2016) studied the dynamic responses of a free-standing bridge pylon under coupled wave and wind actions in a wind tunnel and wave flume. Ma *et al*. (2019) experimentally investigated the across-wind aerodynamic behavior of a bridge tower using a 1:30 scale sectional model and a 1:80 scale aeroelastic model. Siringoringo and Fujino (2012) observed the wind-induced response of an H-shaped suspension bridge tower. The analytical results showed that different wind speeds and wind directions produced different characteristics of the along-wind vibration. These studies produced valuable information on

∗Corresponding author, Ph.D., Lecturer
E-mail: jieao115@163.com
[a]Professor, Ph.D.
E-mail: ljw@gl.chd.edu.cn

ISSN: 1226-6116 (Print), 1598-6225 (Online)

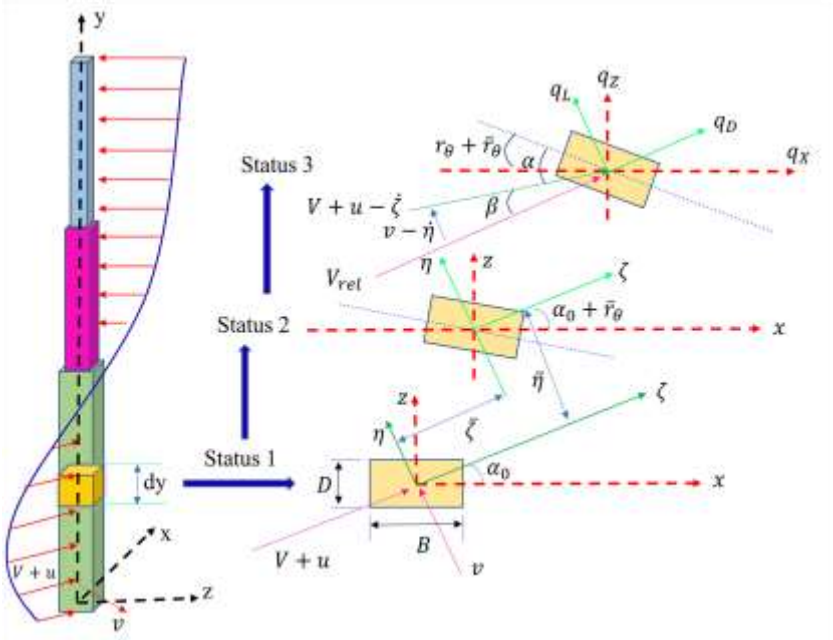

Fig. 1 Variable cross-section pylon under the twisted wind profile

wind-induced pylon vibration. However, no significant information can be gained from the literature on the wind-induced response of a bridge tower under twisted wind profiles.

Prandtl proposed the logarithmic law boundary layer of the fluid flowing over a flat plate. Generally, the logarithmic is also applicable in the strong wind condition of a homogeneous terrain. Nevertheless, numerous numerical studies have shown that wind profiles under a complex terrain do not satisfy the logarithmic law and that wind profiles at different locations are quite different (Cao *et al*. 2012, Abdi and Bitsuamlak 2014, Liu *et al*. 2016, Han *et al*. 2018, Ren *et al*. 2018). Moreover, the results of the wind tunnel test also showed that the wind profiles in a complex terrain are twisted (Li *et al*. 2010, Hu *et al*. 2015, Hu *et al*. 2017, Li *et al*. 2017). However, most of the field-measured wind profile analysis focuses on typhoons and tropical cyclones, and a few studies have analyzed the measured twisted wind profiles in a complex terrain in the monsoon region (Tse *et al*. 2013, He *et al*. 2016, Shu *et al*. 2017).

Motivated by these remaining problems, the objectives of this paper were to investigate the buffeting responses of a variable-cross-section bridge pylon in a trumpet-shaped mountain pass. To achieve this purpose, the quasi-steady theory was used to derive the aerodynamic stiffness, aerodynamic damping and buffeting force matrix under twisted wind profiles. Furthermore, the bridge tower was divided into six segments. The static coefficients at the middle position of segments at different wind yaw angles were calculated by computational fluid dynamics. Then, the measured wind profile and turbulence characteristics were discussed. Based on the measured wind characteristics, the multimode coupled buffeting response of the bridge pylon was calculated in the frequency domain. Finally, the buffeting response of the bridge tower under different wind characteristics was discussed, and some new findings were presented.

2. Theory of buffeting under the twisted wind profile

Generally, a bridge pylon has a variable cross-section. The twisted wind profile defined in this paper contains two cases: (1) the wind speed does not satisfy the power law along the pylon axis, and (2) the variation of the wind direction along the pylon axis is obviously greater than that of the combined action of the Coriolis force, static friction and pressure gradient in a homogeneous terrain. Thus, the twisted wind profile contains the twisted wind speed profile and twisted wind direction profile. To estimate the buffeting response of the pylon, the linear quasi-steady theory is applied. The linear quasi-steady theory cannot take into account the effects of fluid memory (Wu and Kareem 2013, Kavrakov and Morgenthal 2017). The flutter derivatives and aerodynamic admittance functions have been propose to account for fluid memory effects (Davenport 1962, Scanlan and Tomo 1971). However, at high wind speeds, the quasi-steady theory is approximately satisfied (Chen and Kareem 2002). This paper focuses on the buffeting response of a pylon under strong wind conditions; thus, the quasi-steady theory can be partially satisfied.

The wind direction changes along the axial direction of the bridge pylon are defined as α(y). Therefore, the movement of a pylon section under an incidence angle of α_0 is as shown in Fig. 1.

where V is the horizontal velocity, u and v are the longitudinal and lateral fluctuating wind speeds respectively, r_θ is the fluctuating torsional displacement of the structure in the global coordinate system, and $\bar{r}_\theta$ is the average torsional displacement of the structure due to the wind load. In the body coordinate system, the x-axis is taken along the bridge beam axis direction, the z-axis is the

lateral direction, and the y-axis is the bridge pylon axis. In the wind axis coordinate system, ζ and η are the drag force direction and the lift force direction, respectively. According to the Bernoulli equation, the drag, lift and moment forces in the wind coordinate system are given by

$$\begin{bmatrix} q_D(y,t) \\ q_L(y,t) \\ q_M(y,t) \end{bmatrix} = \frac{1}{2}\rho V_{rel}^2 \begin{bmatrix} D(y)C_D(a,y) \\ B(y)C_L(a,y) \\ B(y)^2 C_M(a,y) \end{bmatrix} \tag{1}$$

where V_{rel} the instantaneous relative wind speed. D(y) and B(y) are the cross-sectional width and height, respectively. $C_D(a, y)$, $C_L(a, y)$, and $C_M(a, y)$, are the static coefficients with a wind attack angle α.

$$V_{rel}^2 \approx V^2 + 2Vu - 2V\dot{\varsigma} \tag{2}$$

Transformed into body coordinates:

$$q_{tol}(y,t) = \begin{bmatrix} q_x(a,y) \\ q_z(a,y) \\ q_\theta(a,y) \end{bmatrix} = \begin{bmatrix} \cos(\alpha+\beta) & -\sin(\alpha+\beta) & 0 \\ \sin(\alpha+\beta) & \cos(\alpha+\beta) & 0 \\ 0 & 0 & 1 \end{bmatrix} \begin{bmatrix} q_D(a,y) \\ q_L(a,y) \\ q_M(a,y) \end{bmatrix} \tag{3}$$

where α is expressed as

$$\alpha = \alpha_0 + \overline{r}_\theta + r_\theta \tag{4}$$

where β is the change in instantaneous angle caused by fluctuating wind and structural oscillations, which can be calculated by the following formula

$$\beta = \arctan\left(\frac{v-\dot{\eta}}{V+u-\dot{\varsigma}}\right) \tag{5}$$

Compared with V, μ and $\dot{\varsigma}$ are small. Since β is also small, the following is obtained

$$\sin\beta = \tan\beta = \beta \approx \frac{v-\dot{\eta}}{V} \tag{6}$$

Substitution of Eq. (6) into Eq. (3) leads to

$$\begin{bmatrix} q_x(a,y) \\ q_z(a,y) \\ q_\theta(a,y) \end{bmatrix} = \begin{bmatrix} \cos\alpha & -\sin\alpha & 0 \\ \sin\alpha & \cos\alpha & 0 \\ 0 & 0 & 1 \end{bmatrix} \begin{bmatrix} 1 & -\frac{v-\dot{\eta}}{V} & 0 \\ \frac{v-\dot{\eta}}{V} & 1 & 0 \\ 0 & 0 & 1 \end{bmatrix} \begin{bmatrix} q_D(a,y) \\ q_L(a,y) \\ q_M(a,y) \end{bmatrix} \tag{7}$$

The load vector under the instantaneous wind angle of attack can be expressed as

$$\begin{bmatrix} C_D(a,y) \\ C_L(a,y) \\ C_M(a,y) \end{bmatrix} = \begin{bmatrix} C_D(\overline{\alpha},y) \\ C_L(\overline{\alpha},y) \\ C_M(\overline{\alpha},y) \end{bmatrix} + \alpha_f \begin{bmatrix} C_D'(\overline{\alpha},y) \\ C_L'(\overline{\alpha},y) \\ C_M'(\overline{\alpha},y) \end{bmatrix} \tag{8}$$

where

$$\alpha_f = r_\theta + \frac{v}{V} - \frac{\dot{\eta}}{V} \tag{9}$$

$$\overline{\alpha} = \alpha_0 + \overline{r}_\theta \tag{10}$$

where r_θ and $\overline{r}_\theta$ are small quantities. Combining Eqs. (1)-(10)

$$\begin{bmatrix} q_x(a,y) \\ q_z(a,y) \\ q_\theta(a,y) \end{bmatrix} = \begin{bmatrix} \cos\alpha_0 & -\sin\alpha_0 & 0 \\ \sin\alpha_0 & \cos\alpha_0 & 0 \\ 0 & 0 & 1 \end{bmatrix} \begin{bmatrix} 1 & -\frac{v-\dot{\eta}}{V} & 0 \\ \frac{v-\dot{\eta}}{V} & 1 & 0 \\ 0 & 0 & 1 \end{bmatrix} \frac{1}{2}\rho(V^2+2Vu-2V\dot{\varsigma}) \left(\begin{bmatrix} D(y)C_D(\alpha_0,y) \\ B(y)C_L(\alpha_0,y) \\ B(y)^2 C_M(\alpha_0,y) \end{bmatrix} + \alpha_f \begin{bmatrix} D(y)C_D'(\alpha_0,y) \\ B(y)C_L'(\alpha_0,y) \\ B(y)^2 C_M'(\alpha_0,y) \end{bmatrix} \right) \tag{11}$$

Ignoring the high-order terms, the static force, buffeting force, aerodynamic damping and aerodynamic stiffness are given as

$$\begin{bmatrix} \overline{q}_x(\alpha_0,y) \\ \overline{q}_z(\alpha_0,y) \\ \overline{q}_\theta(\alpha_0,y) \end{bmatrix} = \frac{1}{2}\rho B(y)V^2 \begin{bmatrix} \cos\alpha_0 & -\sin\alpha_0 & 0 \\ \sin\alpha_0 & \cos\alpha_0 & 0 \\ 0 & 0 & 1 \end{bmatrix} \begin{bmatrix} D(y)/B(y)C_D(\alpha_0,y) \\ C_L(\alpha_0,y) \\ B(y)C_M(\alpha_0,y) \end{bmatrix} \tag{12}$$

$$\mathbf{B_q}(\alpha_0,y) = \frac{1}{2}\rho VB(y)\mathbf{b_q}(\alpha_0,y)\begin{bmatrix} u \\ v \end{bmatrix} \tag{13}$$

$$\mathbf{b_q}(\alpha_0,y) = \begin{bmatrix} \cos\alpha_0 & -\sin\alpha_0 & 0 \\ \sin\alpha_0 & \cos\alpha_0 & 0 \\ 0 & 0 & 1 \end{bmatrix} \begin{bmatrix} 2D(y)/B(y)C_D(\alpha_0,y) & (D(y)/B(y))C_D'(\alpha_0,y)-C_L(\alpha_0,y) \\ 2C_L(\alpha_0,y) & (D(y)/B(y))C_D(\alpha_0,y)+C_L'(\alpha_0,y) \\ 2B(y)C_M(\alpha_0,y) & B(y)C_M'(\alpha_0,y) \end{bmatrix} \tag{14}$$

$$\mathbf{C_{ae}}(\alpha_0,y) = -\frac{1}{2}\rho VB(y) \begin{bmatrix} \cos\alpha_0 & -\sin\alpha_0 & 0 \\ \sin\alpha_0 & \cos\alpha_0 & 0 \\ 0 & 0 & 1 \end{bmatrix} \begin{bmatrix} 2D(y)/B(y)C_D(\alpha_0,y) & D(y)/B(y)C_D'(\alpha_0,y)-C_L(\alpha_0,y) & 0 \\ 2C_L(\alpha_0,y) & D(y)/B(y)C_D(\alpha_0,y)+C_L'(\alpha_0,y) & 0 \\ 2B(y)C_M(\alpha_0,y) & B(y)C_M'(\alpha_0,y) & 0 \end{bmatrix} \begin{bmatrix} \dot{\varsigma} \\ \dot{\eta} \\ \dot{r}_\theta \end{bmatrix} \tag{15}$$

$$\mathbf{K_{ae}}(\alpha_0,y) = \frac{1}{2}\rho V^2 B(y) \begin{bmatrix} \cos\alpha_0 & -\sin\alpha_0 & 0 \\ \sin\alpha_0 & \cos\alpha_0 & 0 \\ 0 & 0 & 1 \end{bmatrix} \begin{bmatrix} 0 & 0 & D(y)/B(y)C_D'(\alpha_0,y) \\ 0 & 0 & C_L'(\alpha_0,y) \\ 0 & 0 & B(y)C_M'(\alpha_0,y) \end{bmatrix} \begin{bmatrix} \varsigma \\ \eta \\ r_\theta \end{bmatrix} \tag{16}$$

According to the geometric relationship, the coordinate transformation relationship between the wind axis and body axis coordinate system is as follows

$$\begin{bmatrix} \dot{\varsigma} \\ \dot{\eta} \\ \dot{r}_\theta \end{bmatrix} = \begin{bmatrix} \cos\alpha_0 & \sin\alpha_0 & 0 \\ -\sin\alpha_0 & \cos\alpha_0 & 0 \\ 0 & 0 & 1 \end{bmatrix} \begin{bmatrix} \dot{r}_x \\ \dot{r}_z \\ \dot{r}_\varphi \end{bmatrix} \tag{17}$$

By introducing Eq. (17) into Eq. (15), the aerodynamic damping matrix of the pylon section can be obtained

$$\mathbf{C_{ae}}(\alpha_0,y) = -\frac{1}{2}\rho VB(y) \begin{bmatrix} \cos\alpha_0 & -\sin\alpha_0 & 0 \\ \sin\alpha_0 & \cos\alpha_0 & 0 \\ 0 & 0 & 1 \end{bmatrix} \begin{bmatrix} 2D(y)/B(y)C_D(\alpha_0,y) & D(y)/B(y)C_D'(\alpha_0,y)-C_L(\alpha_0,y) & 0 \\ 2C_L(\alpha_0,y) & D(y)/B(y)C_D(\alpha_0,y)+C_L'(\alpha_0,y) & 0 \\ 2B(y)C_M(\alpha_0,y) & B(y)C_M'(\alpha_0,y) & 0 \end{bmatrix} \begin{bmatrix} \cos\alpha_0 & \sin\alpha_0 & 0 \\ -\sin\alpha_0 & \cos\alpha_0 & 0 \\ 0 & 0 & 1 \end{bmatrix} \begin{bmatrix} \dot{r}_x \\ \dot{r}_z \\ \dot{r}_\varphi \end{bmatrix} \tag{18}$$

Similarly, the aerodynamic stiffness matrix can be obtained

$$\mathbf{K_{ae}}(\alpha_0,y) = \frac{1}{2}\rho V^2 B(y) \begin{bmatrix} \cos\alpha_0 & -\sin\alpha_0 & 0 \\ \sin\alpha_0 & \cos\alpha_0 & 0 \\ 0 & 0 & 1 \end{bmatrix} \begin{bmatrix} 0 & 0 & D(y)/B(y)C_D'(\alpha_0,y) \\ 0 & 0 & C_L'(\alpha_0,y) \\ 0 & 0 & B(y)C_M'(\alpha_0,y) \end{bmatrix} \begin{bmatrix} \cos\alpha_0 & \sin\alpha_0 & 0 \\ -\sin\alpha_0 & \cos\alpha_0 & 0 \\ 0 & 0 & 1 \end{bmatrix} \begin{bmatrix} r_x \\ r_z \\ r_\varphi \end{bmatrix} \tag{19}$$

The dynamic equation of the bridge pylon, considering the mass, self-exciting force and buffeting force along the pylon axis in the generalized coordinate system, is as follows

$$\tilde{\mathbf{M}}\ddot{\boldsymbol{\eta}}(t) + (\tilde{\mathbf{C}} - \tilde{\mathbf{C}}_{\mathbf{ae}})\dot{\boldsymbol{\eta}}(t) + (\tilde{\mathbf{K}} - \tilde{\mathbf{K}}_{\mathbf{ae}})\boldsymbol{\eta}(t) = \tilde{\mathbf{R}}(t) \tag{20}$$

$$\tilde{\mathbf{M}} = \int_{\mathrm{L}} \boldsymbol{\varphi}^{\mathrm{T}}(y)\mathbf{M}(y)\boldsymbol{\varphi}(y)dy \tag{21}$$

$$\tilde{\mathbf{C}}_{\mathbf{ae}} = \int_{\mathrm{L}} \boldsymbol{\varphi}^{\mathrm{T}}(y)\mathbf{C}_{\mathbf{ae}}(y)\boldsymbol{\varphi}(y)dy \tag{22}$$

$$\tilde{\mathbf{K}}_{\mathbf{ae}} = \int_{\mathrm{L}} \boldsymbol{\varphi}^{\mathrm{T}}(y)\mathbf{K}_{\mathbf{ae}}(y)\boldsymbol{\varphi}(y)dy \tag{23}$$

where $\tilde{M}$, $\tilde{C}$ and $\tilde{K}$ are the structural modal mass, modal damping, and modal stiffness matrix, respectively. $\tilde{C}_{\mathrm{ae}}$ is the modal aerodynamic damping and $\tilde{K}_{\mathrm{ae}}$ is the modal aerodynamic stiffness. $\tilde{R}(t)$ is the modal buffeting forcevector, and $\eta(t)$ is the generalized coordinates. $\boldsymbol{\varphi}(y)$ is the modal coordinates, and $\boldsymbol{\eta}(t)$ denotes the matrix transpose operator. The influence of the variable cross-section and the wind direction changes with height will be considered. A Fourier transform is performed on Eq. (20) to obtain Eq. (24).

$$\left[-\tilde{\mathbf{M}}\omega^2 + (\tilde{\mathbf{C}} - \tilde{\mathbf{C}}_{\mathbf{ae}})\mathrm{i}\,\omega + (\tilde{\mathbf{K}} - \tilde{\mathbf{K}}_{\mathbf{ae}})\right]\boldsymbol{\eta}(\omega) = \tilde{\mathbf{R}}(\omega) \tag{24}$$

For the variable-section bridge pylon, the turbulence spectral density matrix and buffeting force spectral density of the arbitrary two-point are expressed as follows (Cheynet *et al*. 2016)

$$\mathbf{S}(y_1, y_2, \omega) = \begin{bmatrix} \mathbf{S}_{\mathbf{uu}}(y_1, y_2, \omega) & \mathbf{S}_{\mathbf{uv}}(y_1, y_2, \omega) \\ \mathbf{S}_{\mathbf{vu}}(y_1, y_2, \omega) & \mathbf{S}_{\mathbf{vv}}(y_1, y_2, \omega) \end{bmatrix} \tag{25}$$

$$\mathbf{S}_{\mathbf{qq}}(y_1, y_2, \omega) = \left(\frac{\rho V}{2}\right)^2 B(y_1)B(y_2)\mathbf{b}_{\mathbf{q}}(y_1)\mathbf{S}(y_1, y_2, \omega)\mathbf{b}_{\mathbf{q}}^{\mathbf{T}}(y_2) \tag{26}$$

where $\mathbf{S}(y_1, y_2, \omega)$ is the fluctuating wind spectral density matrix, which contains auto-spectral and cross-spectral densities at the two points y_1 and y_2. The cross-spectral densities are ignored in this study. Then, the buffeting force spectrum matrix $\mathbf{S}_{\tilde{\mathbf{R}}}(\omega)$ is expressed as follows

$$\boldsymbol{S}_{\tilde{\mathrm{R}}}(\omega) = \begin{bmatrix} S_{\tilde{R}1}S_{\tilde{R}1}(\omega) & \cdots & S_{\tilde{R}1}S_{\tilde{R}m}(\omega) & \cdots & S_{\tilde{R}1}S_{\tilde{R}r}(\omega) \\ \vdots & \ddots & \vdots & \iddots & \vdots \\ S_{\tilde{R}n}S_{\tilde{R}1}(\omega) & \cdots & S_{\tilde{R}n}S_{\tilde{R}m}(\omega) & \cdots & S_{\tilde{R}n}S_{\tilde{R}r}(\omega) \\ \vdots & \iddots & \vdots & \ddots & \vdots \\ S_{\tilde{R}r}S_{\tilde{R}1}(\omega) & \cdots & S_{\tilde{R}r}S_{\tilde{R}m}(\omega) & \cdots & S_{\tilde{R}r}S_{\tilde{R}r}(\omega) \end{bmatrix} \tag{27}$$

where r is the modal number, and $S_{\tilde{R}n}S_{\tilde{R}m}(\omega)$ is defined as follows

$$S_{\tilde{R}n}S_{\tilde{R}m}(\omega) = \frac{\iint_{L} \boldsymbol{\varphi}_{\mathbf{n}}^{\mathbf{T}}(y_1)\mathbf{S}_{\mathbf{qq}}(y_1, y_2, \omega)\boldsymbol{\varphi}_{\mathbf{m}}(y_2)dy_1dy_2}{(\omega_n^2\tilde{M}_n)(\omega_m^2\tilde{M}_m)} \tag{28}$$

Defining the frequency response function as $\mathbf{H}_{\boldsymbol{\eta}}(\omega)$, the response spectrum $\mathbf{S}_{\boldsymbol{\eta}}(\omega)$ can be expressed as

$$\mathbf{S}_{\boldsymbol{\eta}}(\omega) = \mathbf{H}_{\boldsymbol{\eta}}^{*}\mathbf{S}_{\tilde{\mathbf{R}}}(\omega)\mathbf{H}_{\boldsymbol{\eta}}^{\mathbf{T}} \tag{29}$$

$$\mathbf{H}(\omega) = \left\{\mathrm{I} - \tilde{\mathbf{K}}^{-1}\tilde{\mathbf{K}}_{\mathbf{ae}} - \mathrm{diag}\left[\frac{1}{\omega_n^2}\right]\omega^2 + \left\{\mathrm{diag}\left[\frac{2\xi_n}{\omega_n}\right] - \tilde{\mathbf{K}}^{-1}\tilde{\mathbf{C}}_{\mathbf{ae}}\right\}\mathrm{i}\,\omega\right\}^{-1} \tag{30}$$

Therefore, the buffeting response spectrum at y_r is

$$\mathbf{S}_{\mathbf{rr}}(y_r, \omega) = \boldsymbol{\varphi}_{\mathbf{r}}(y_r)\mathbf{S}_{\boldsymbol{\eta}}(\omega)\boldsymbol{\varphi}_{\mathbf{r}}^{\mathbf{T}}(y_r) \tag{31}$$

3. Bridge site and monitoring system

The bridge site is a trumpet-shaped mountain pass on the Loess Plateau. It has the following two characteristics: (1) The bridge site is at the junction of mountains and valleys. The terrain on both sides is completely different. The mountains cause airflow backflow at the bridge site. (2) The terrain has an expanding effect on the northwest wind and a compression effect on the southeast wind. Until now, there have been few observations of the wind characteristics of this type of terrain. To study the wind characteristics of the bridge site, a 60 m mast was built on the flat terrain of the bridge site. The mast was equipped with a two-dimensional ultrasonic anemometer (2D Gill Wind Sonic) at heights of 10 m, 20 m and 45 m, and two 2D anemometers were mounted on the platform at a height of 30 m with a horizontal distance of 18 m. The wind data can simultaneously write to a file and give diagnostic values. To reduce the impact of the mast on the wind observation data, the anemometers were extended out of the mast. Simultaneously, a phased-array doppler sodar(PDS), which was developed by ART (Atmospheric Research & Technology), was installed upstream of the bridge site. It can observe the wind speed and direction within a height of 300 m. The sampling frequency of the 2D wind observer is 4 HZ. The 2D wind data collected for 345 days were analyzed. The PDS collected 209 days of data. The surrounding topography of the bridge site and wind mast layout at the bridge site are shown in Fig. 2.

4. Wind data analysis

4.1 Mean wind characteristics

According to the literature, the wind record was divided into 10 min segments without overlapping, and segments with a mean wind speed of no less than 10 m/s were obtained (Masters *et al.* 2010). A total of 2415 strong wind samples satisfied the condition. The relationships between the wind speed, wind direction and terrain are shown in Fig. 3. Fig. 3 shows that the strong wind direction is obviously affected by the terrain. The wind direction is mainly

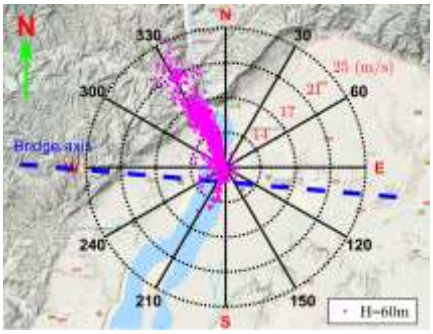

Fig. 3 Wind rose

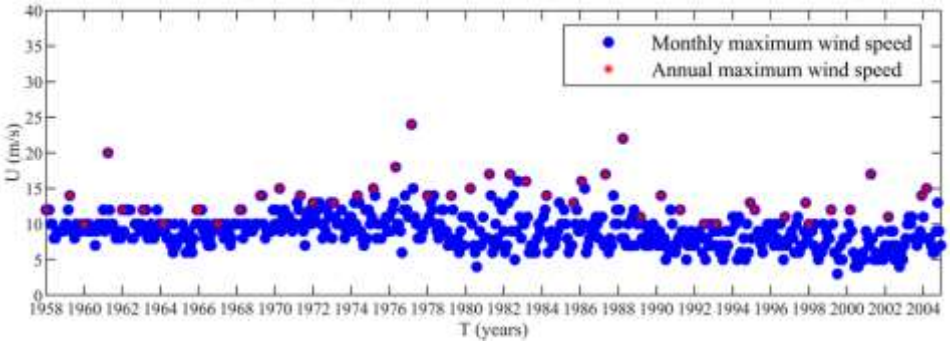

Fig. 4 Extreme wind speed

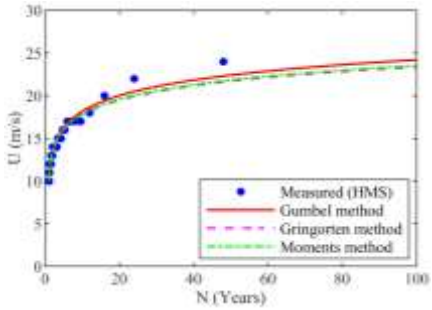

Fig. 5 Wind speed return period (Year)

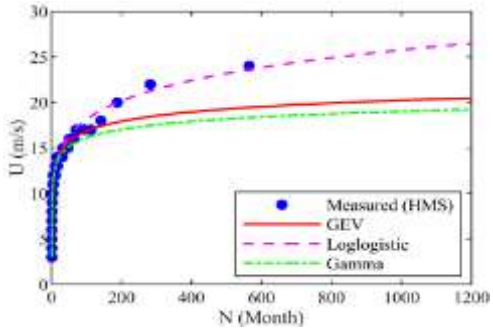

Fig. 7 Wind speed return period (Month)

concentrated at 330° and 210°, which correspond to upstream and downstream of the river. The upstream wind speed is significantly stronger than the downstream wind speed.

The maximum wind speed of the Hejin Meteorological Station (HMS) for 47 consecutive years is shown in Fig. 4.

The relationship between the return period and the cumulative probability density is as follows

$$N = \frac{1}{1 - F_U(U)} \tag{32}$$

where N is the return period, and $F_u(U)$ is the cumulative probability distribution. According to the generalized extreme value I (GEV) distribution, the wind speeds of the different return periods calculated by different methods are shown in Fig. 5(Gumbel 1954, Gringorten 1963, Holmes2018). Fig. 5 shows that the wind speed calculated by the Gumbel method is the largest, and the wind speed of the 100-year return period is 24.2 m/s. However, Fig. 5 also shows that using the generalized extreme value distribution may underestimate the return wind speed. In fact, the annual extreme wind speed does not satisfy the generalized extreme value I distribution in this terrain. According to the loglikelihood test, the optimal fit distribution of the monthly and annual maximum wind speeds is the log-logistic distribution. In Figs. 6(a) and 6(b), the histogram plots of the monthly and annual maximum wind speeds are shown together with the fitted probability density functions. Because the annual maximum wind speed sample is small, it is considered that the monthly maximum wind speed can be used to estimate the the extreme wind speed in the recurrence period (Grigoriu 1984). Therefore, the recurring wind speed under each distribution type is shown in Fig. 7.

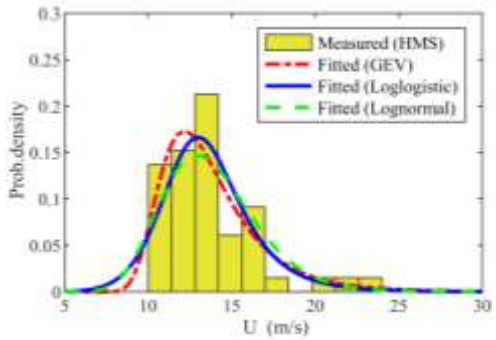

(a) Probability distribution of the annual maximum wind speed

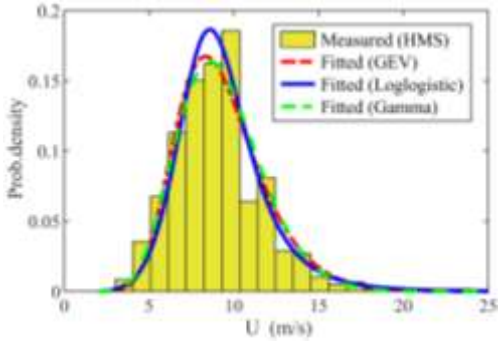

(b) Probability distribution of the monthly maximum wind speed

Fig. 6 Probability distributions of the maximum wind speed

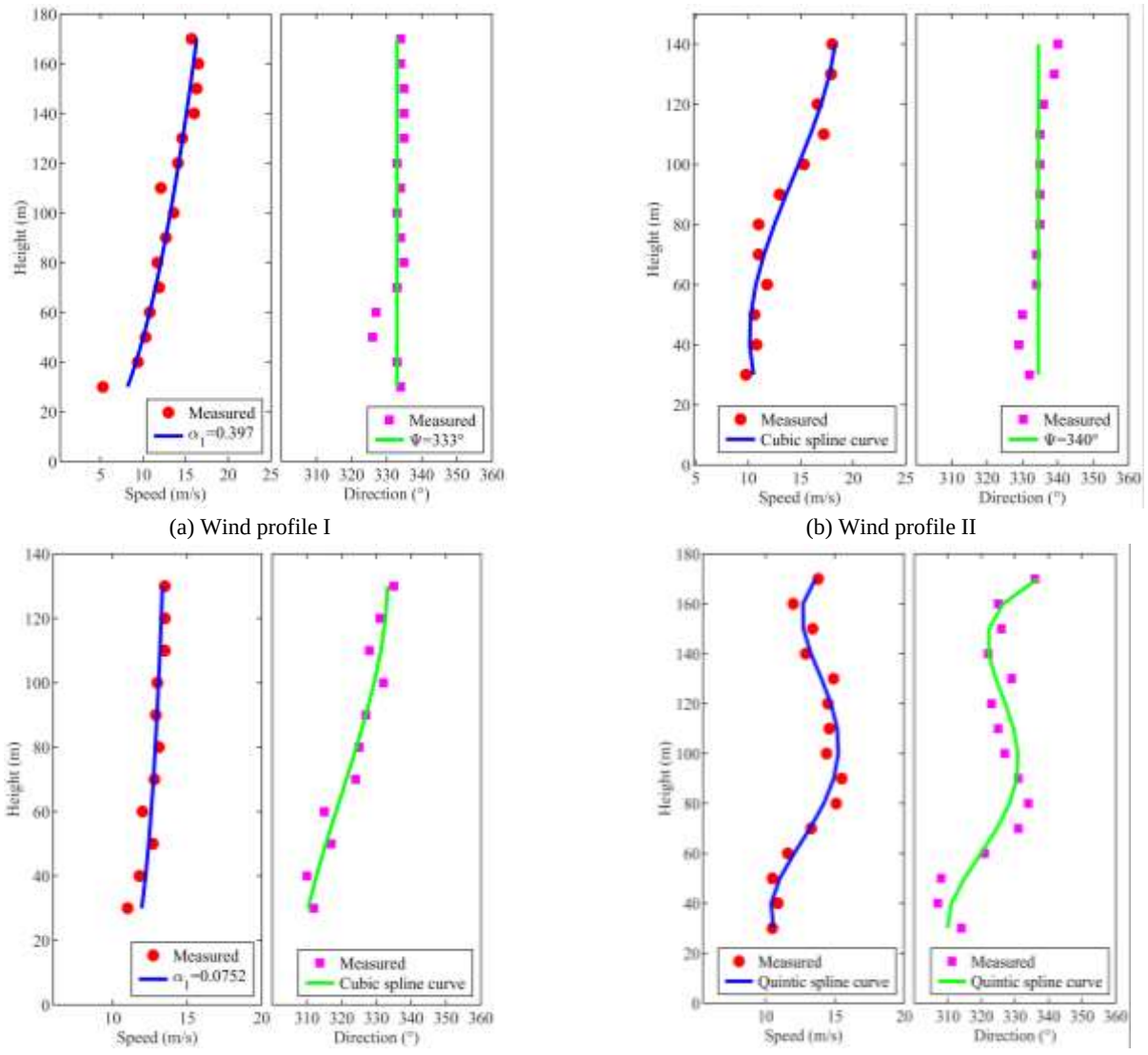

Fig. 8 Measured wind profiles

Fig. 7 shows that the log-logistic distribution can be used to estimate the wind speed during the return period. The wind speed of the 100- year return period is 26.5 m/s. The wind data of the PDS are analyzed to study the wind profile characteristics. The maximum observation height of the sodar is 200 m in this study. Fig. 8 shows several typical wind profiles in the strong wind environment. The power function was used as the objective function to fit the wind speed profile satisfying the power law, and the wind speed profile that did not satisfy the power law was fitted with a spline curve.

Wind profiles I and III satisfy the exponential law. The wind yaw angles of wind profiles I and II do not vary significantly along the height. Wind profile I is the conventional wind profile. Wind profile IV does not satisfy the exponential law, and the wind yaw angle varies significantly along the height.

To date, few studies have been conducted on the development of the wind field probability descriptions (Fenerci and Øiseth 2018). In this study, a probabilistic description of the measured wind profile was carried out. The samples with average values of wind speeds of all heights greater than 10 m/s were selected. There were 1161 strong wind profile samples. The log-likelihood criterion was used to test the measured wind data. The result indicated that the log-logistic distribution can be optimally fitted. The wind speed and wind direction at the peak of the probability density of each height are connected to form a probabilistic wind profile. The probability wind profile named wind profile V is shown in Fig. 9. It can be clearly observed that the wind direction and wind speed are twisted. The wind speed starts to decelerate at a height of 120 m, and the wind direction abruptly changes at a height of 40 m-70 m.

4.2 Turbulence characteristics

The turbulence spectrum indicates the turbulent energy distribution over the frequency. To date, most wind spectra rely on the assumption of a homogenous terrain, and few

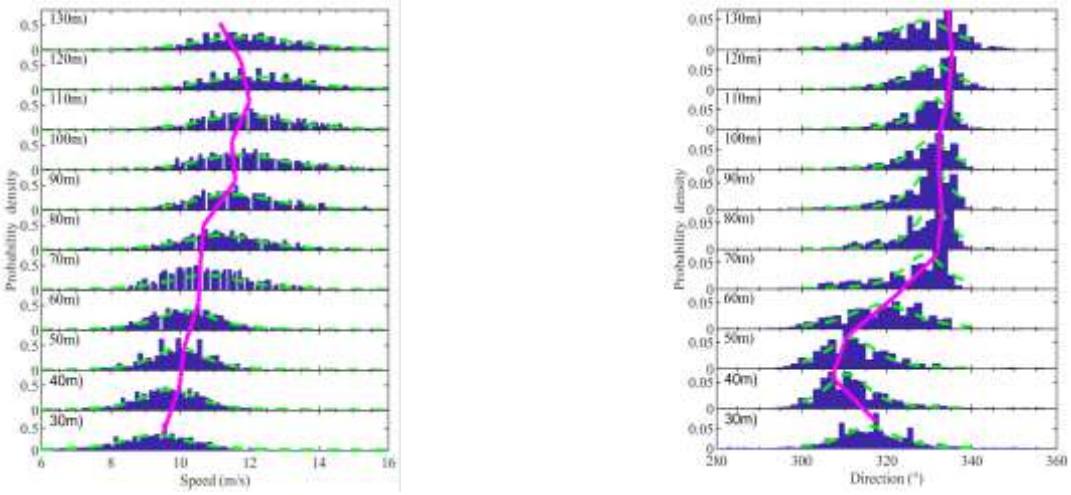

(a) Probability distribution of the wind speed (b) Probability distribution of the wind direction

Fig. 9 Wind profile Ⅴ

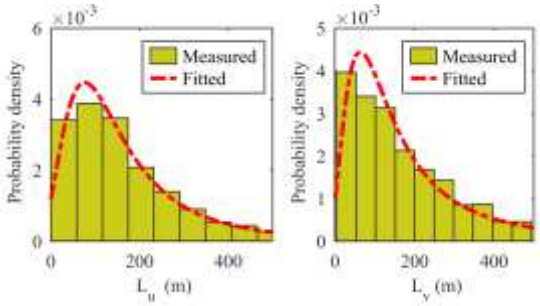

Fig. 10 Probability density of turbulence length scales

studies have fitted the wind spectra based on the measureddata at a trumpet-shaped mountain pass. The measured strong wind data were fitted by the Kaimal-type expression (Fenerci and Øiseth 2017)

$$\frac{nS_i}{\sigma_i^2} = \frac{A_i f_z}{(1+1.5\cdot A_i f_z)^{5/3}} \qquad i = u, v \tag{33}$$

$$f_z = \frac{nL_i}{U} \tag{34}$$

where A_i denotes the coefficients to be determined by the nonlinear least-squares fitting; u and v are the turbulence components; n denotes the frequency in Hz; and z is the height above the ground. L_i denotes the turbulence length scale components in the direction of the main flow. If the turbulence is a stationary stochastic process and Taylor's hypothesis of frozen turbulence is assumed valid, then the turbulence length scales can be estimated using the autocorrelation function. This function can be written as Eq. (35)

$$L_i = \frac{U}{\sigma_i^2}\int_0^b R_i(\tau)\,d\tau \qquad i = u, v \tag{35}$$

where R(τ) is the turbulence cross-covariance function in time and $b = 0.05\sigma^2$ (Flay and Stevenson 1988). The values of the turbulent integral scale were tested by the loglikelihood criterion. It was concluded that the generalized extremum distribution can be optimally fitted. The measured turbulent integral scales and the fitted probability density functions are shown in Fig. 10.

The measured turbulence was divided into eight sections with a 75% overlap, and the Welch method was used to estimate the power spectral density. The average spectrum

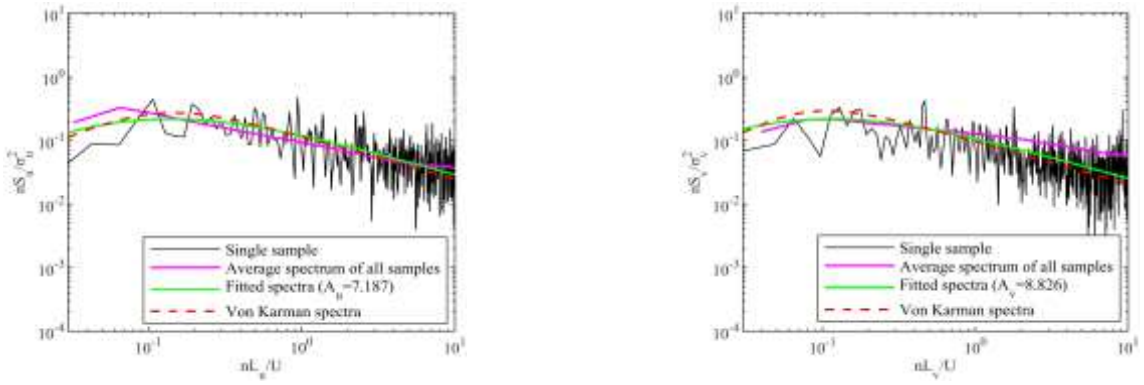

(a) Longitudinal wind spectra (b) Lateral wind spectra

Fig. 11 Measured wind spectra

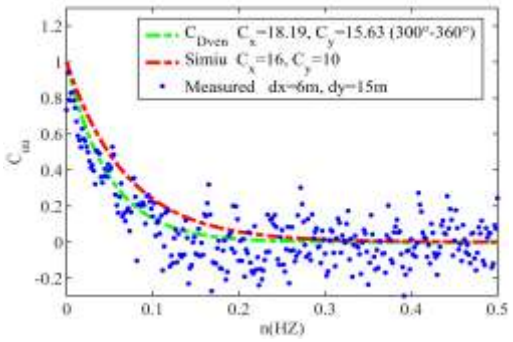

Fig. 12 Normalized cross-spectra

of all samples was obtained. All sample fitting parameters were averaged to obtain the fitted spectrum. The stopping criterion of the fitting was the objective function change of less than 1e-7 during a step. The measured turbulence spectrum was compared with the Von Karman spectrum as shown in Fig. 11.

The normalized cross-spectrum model suggested by A.G Davenport was used here. The anemometer placed on the windward side of the mast may be less affected by the mast. This direction is at an angle of 300°-360°, which is also the direction of strong winds. Therefore, the windward side observation data were selected for normalized cross-spectrum fitting. The decay coefficients were fitted by the

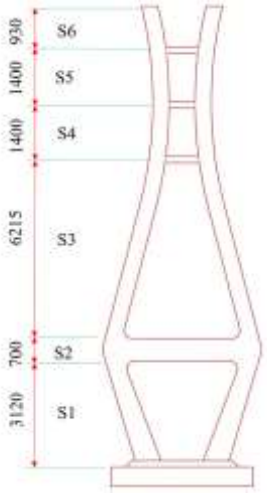

(a) Pylon segmentation diagram

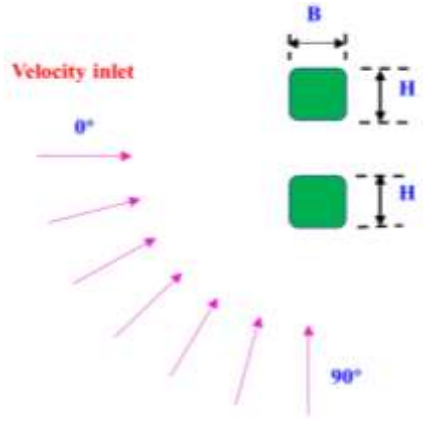

(b) Calculation case

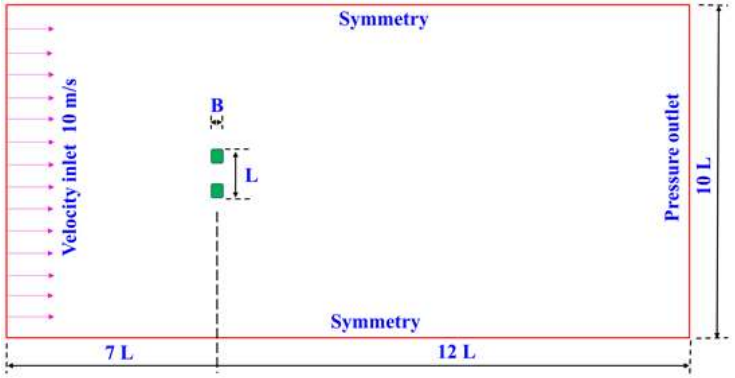

(c) Computational domain

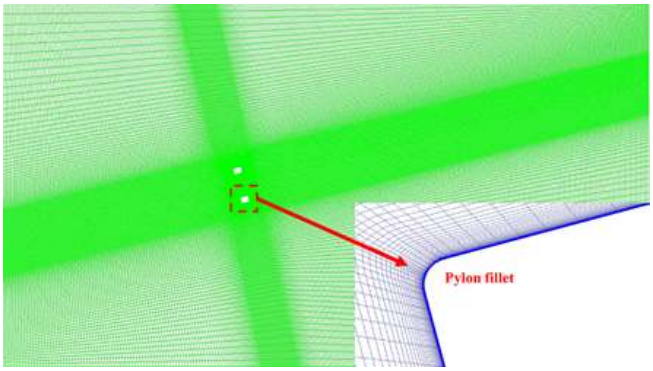

(d) Global mesh and local mesh of S1

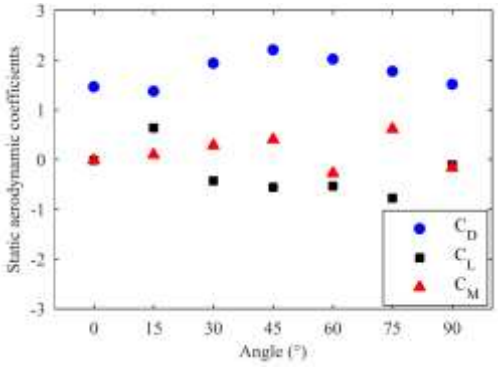

(e) Static aerodynamic coefficients of S1

Fig. 13 CFD calculation of the static coefficient

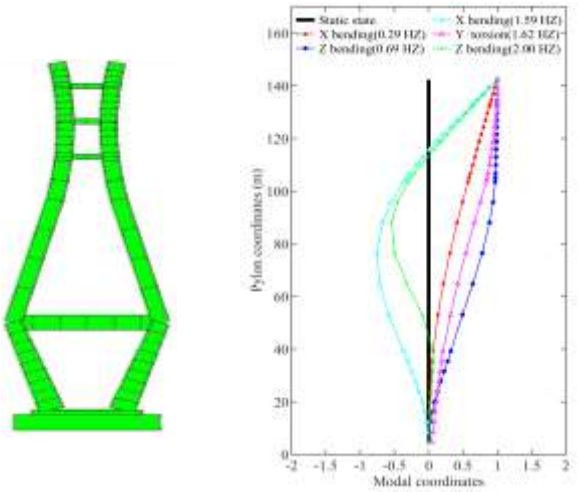

(a) Pylon finite element model

(b) Mode shapes and frequencies

Fig. 14 Dynamic characteristics of the bridge pylon

nonlinear least squares. The results are presented in Fig. 12.

5. Buffeting analysis of the bridge pylon

5.1 Bridge pylon parameters

Since the bridge pylon has a variable section, it was divided into six segments, as shown in Fig. 13(a). The lowest horizontal beam is named segment 2 and is considered in the buffeting response calculation. Because the height of the beam section is small, other horizontal beams are not considered in the buffeting response calculation. However, these horizontal beams are considered in the modal analysis of the pylon. The static aerodynamic coefficients in the middle of the segment were calculated by the computational fluid dynamics (CFD). The turbulence model was the *k*-*ω* shear stress transport (SST) model in this study. The equation was solved using the SIMPLEC algorithm. For the spatial discretization, the second-order upwind scheme was chosen. The value of y+ was one. The first layer of the grid height was 3.8e-5-4.5e-5 m. The inlet was the velocity inlet, and the inlet speed was 10 m/s. The outlet was the pressure outlet. The two sidewalls were the symmetry boundaries (Rocchi *et al*. 2014, Han *et al*. 2016, Li *et al.* 2018). According to the grid-independent verification, the number of grids was approximately 100,000, which can meet the calculation accuracy requirements. The calculation case is shown in Fig. 13(b) The computational domain is shown in Fig. 13(c) and the mesh grid under the 15° yaw angle of the first segment is shown in Fig. 13(d) The static aerodynamic coefficients of the first segment are shown in Fig. 13(e).

The modal analysis of the bridge pylon was performed using ANSYS software. The pylon was modeled by the Beam4 element. The finite element model of the pylon is shown in Fig. 14(a). The typical modal shape and frequencies are shown in Fig. 14(b).

5.2 Buffeting results

5.2.1 Buffeting response of different wind characteristics

The basic wind speed was set to 26.5 m/s in the buffeting response calculation. The strong wind records were mainly approximately 330°. The bridge girder axis was at angle of 280°. Therefore, the yaw angle to the *x*-axis was 50°. For simplicity, the wind speed profile I was selected for the buffeting response calculation. The structural damping ratio was conservatively taken as 0.005. The turbulence integral scale at the peak of the probability density is adopted. The Von Karman spectrum and Simiu decay coefficients were used for the design wind characteristics. The results of the buffeting response under different wind characteristics are shown in Fig. 15. Fig. 15

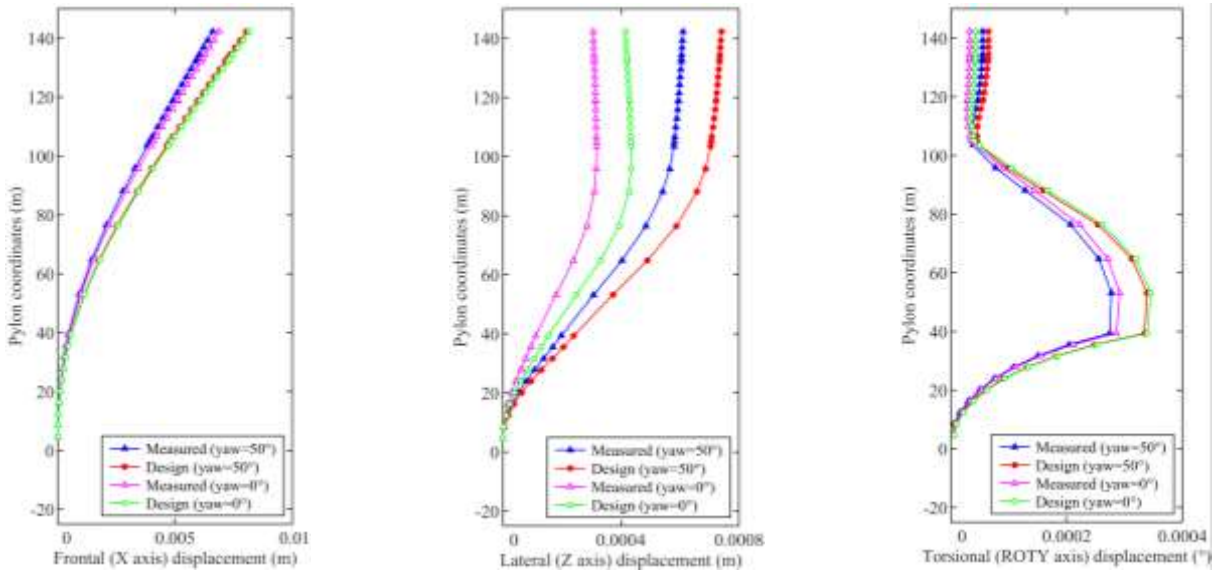

(a) (b) (c)

Fig. 15 Influence of wind characteristics on the buffeting response

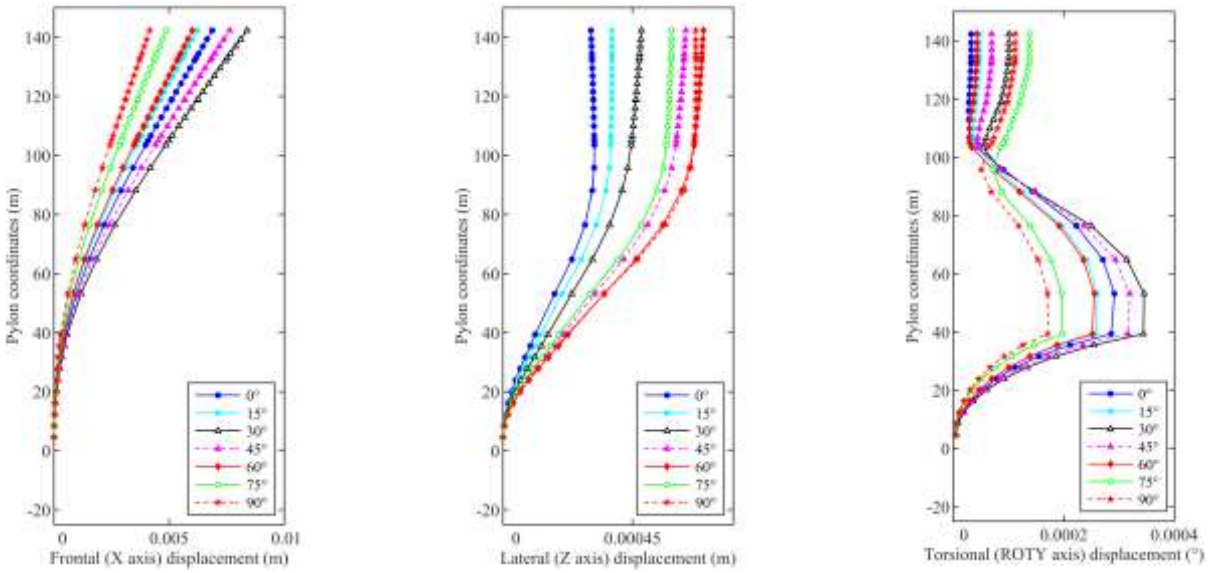

(a) (b) (c)

Fig. 16 Influence of different wind directions on the buffeting response

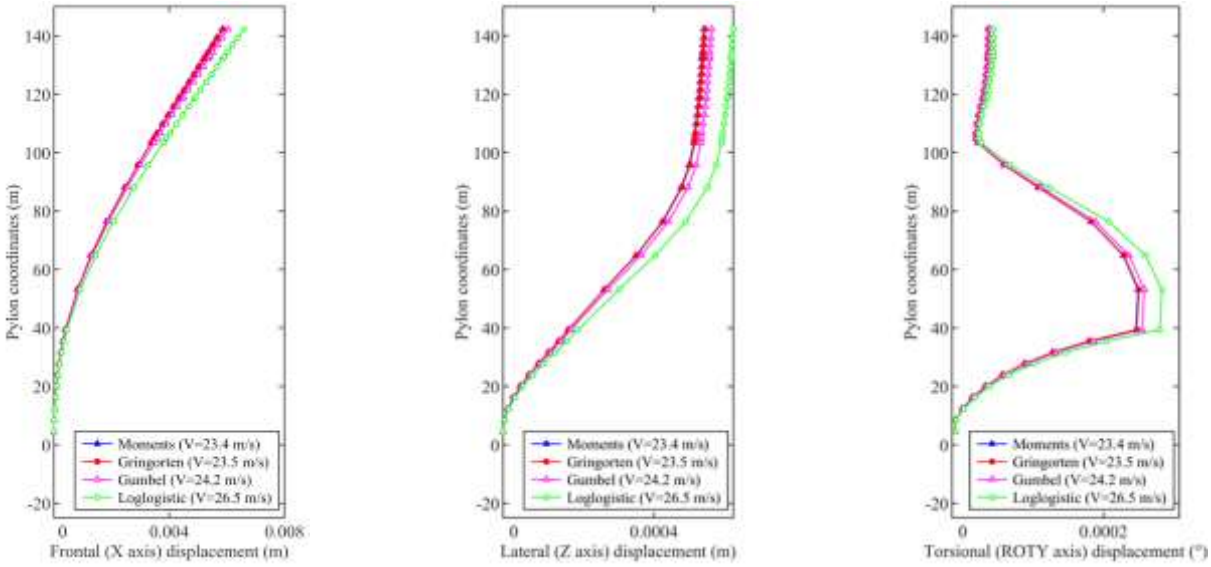

(a) (b) (c)

Fig. 17 Influence of mean speeds on the buffeting response

shows that the buffeting response under the design wind characteristics is larger than the buffeting response under the measured wind characteristics. This result mainly occurred because the energy of the Von Karman spectrum is larger than that of the measured spectrum and because the Simiu decay coefficients overestimate the correlation of the fluctuating wind. It is worth noting that the frontal and torsional buffeting response values are not maximum at a yaw angle of 0°. Therefore, the wind yaw effect should be considered in the buffeting response calculation of a pylon under the conventional wind profile.

5.2.2 Buffeting response of different wind directions

To study the influence of the wind yaw angle on the buffeting response of a pylon under the conventional wind profile, the buffeting response of the pylon under different wind yaw angles was calculated. Wind speed profile I was selected, and the measured wind characteristics were selected. The basic wind speed was 26.5 m/s. The results of the buffeting response under the different wind yaw angles are shown in Fig. 16. The results show that the frontal and torsional buffeting responses are largest at the 30° wind yaw angle. The lateral maximum buffeting response of the pylon occurs at the 90° and 60° wind yaw angles.

5.2.3 Buffeting response of different mean speeds

According to the generalized extreme value I distribution, the wind speed in the return period estimated by different methods is different. Meanwhile, the measured maximum wind speed does not satisfy the generalized

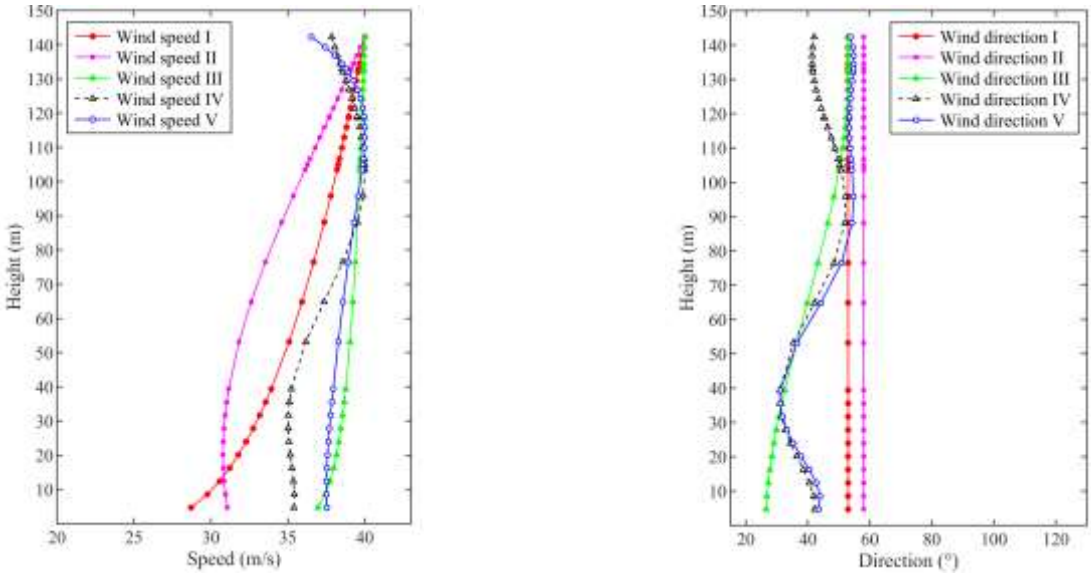

(a) (b)

Fig. 18 The calculated I-V wind profiles

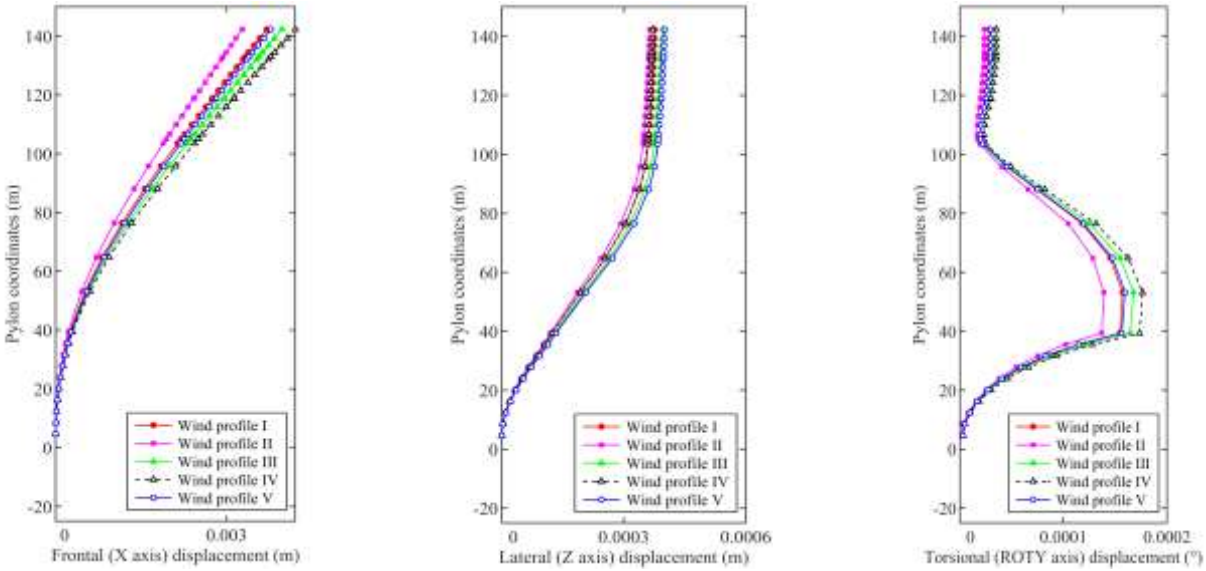

(a) (b) (c)

Fig. 19 Influence of the measured wind profiles on the buffeting response

extreme value I distribution, and the return period wind speed of the log-logistic distribution is different from that of the generalized extreme value I distribution. This section discusses the effect of the different basic wind speeds on the buffeting response of the bridge tower. The initial conditions for the buffeting response calculation are wind speed profile I and the measured wind characteristics. The calculation results in Fig. 17 show that the basic wind speed can significantly affect the pylon buffeting response.

5.2.4 Buffeting response of different wind profiles

Because the measured wind speeds of the five wind profiles were different, there was no uniform standard for comparing the effects on the buffeting response. To unify the wind speed, the maximum wind speed within the height of the pylon under each wind profile was set to 40 m/s. According to the fitting function of five wind profiles, the wind speeds at other heights can be deduced through the maximum wind speed point. The five new wind profiles are named for the calculated wind profile, and this section focuses on their buffeting response. In addition, the bridge axis was at 280°. Therefore, the measured wind direction of the wind profile was necessary to subtract the 280°. The wind profiles after unifying the maximum wind speed are shown in Fig. 18. Since the radar does not measure the wind speed and direction at heights of 10 m and 20 m, it was supplemented by the 30 m radar data. This had little effect on the buffeting response. There were two reasons. First, the wind speed is small at heights of 10 m and 20 m.

Second, the buffeting force at the bottom of the pylon has little effect on the buffeting response. The results of the pylon buffeting response are shown in Fig. 19.

Fig. 19 shows that the maximum frontal and torsional buffeting responses occur in wind profile IV, and that the maximum lateral buffeting responses occur in the wind profile V. The buffeting responses of wind profiles I and II are smaller. The main reason is that the mean wind speeds are smaller than those of the wind profiles, and the wind direction remains constant along the height. However, a high wind speed does not necessarily have the largest buffeting response, such as wind profile Ⅲ. Therefore, the largest buffeting response under the wind profiles IV and V may be mainly due to the severely twisted wind direction profile.

6. Conclusions

The strong wind characteristics and buffeting responses of a free-standing bridge pylon located in a trumpet-shaped mountain pass were studied. The main conclusions are summarized as follows:

- The strong wind direction at a height of 60 m is concentrated at 330°, which is parallel to the river valley direction. The extreme wind speed does not satisfy the generalized extreme value I distribution in this terrain, and the generalized extreme value I distribution will underestimate the extreme wind speed. The basic wind speed during the 100-year return period is 26.5 m/s by the log-logistic distribution.
- The measured wind profile shows that the wind profiles can be divided into four categories, and the probabilistic wind profile (profile V) indicates that the wind profile does not satisfy the power law. The wind speed profile and wind direction profile are severely twisted.
- The value of the Von Karman spectra in both the longitudinal and lateral directions are greater than the measured wind spectra value. The decay coefficients suggested by Simiu will overestimate the turbulence correlation.
- The buffeting response of a pylon is affected by the turbulence wind characteristics, mean wind speeds, wind yaw angles and wind profiles. Under the general wind profile I, the peak buffeting response of the pylon is not in the frontal and lateral wind yaw directions of the bridge tower. The estimation of the buffeting response of a pylon during construction requires consideration of the twisted wind profile effects.

Acknowledgements

The research described in this paper was financially supported by the National Natural Science Foundation of China (Grant Nos. 51978077 and 51808052), Fundamental Research Funds for the Central Universities (300102219531).

References

Abdi, D.S. and Bitsuamlak, G.T. (2014), "Wind flow simulations on idealized and real complex terrain using various turbulence models", *Adv. Eng. Software*. **75**, 30-41. https://doi.org/10.1016/j.advengsoft.2014.05.002.

Cao, S., Wang, T., Ge, Y. and Tamura, Y. (2012), "Numerical study on turbulent boundary layers over two-dimensional hills—effects of surface roughness and slope", *J. Wind Eng. Ind. Aerod*., **104**, 342-349. https://doi.org/10.1016/j.jweia.2012.02.022.

Chen, X. and Kareem, A. (2002), "Advances in modeling of aerodynamic forces on bridge decks", *J. of Eng. Mech*. **128**(11), 1193-1205. https://doi.org/10.1061/(ASCE)07339399(2002)128:11(1193).

Cheynet, E., Jakobsen, J.B. and Snæbjörnsson, J. (2016), "Buffeting response of a suspension bridge in complex terrain", *Eng. Struct*., **128**, 474-487. https://doi.org/10.1016/j.engstruct.2016.09.060.

Davenport, A.G. (1962), "Buffeting of a suspension bridge by storm winds", *J. Struct. Div*., **88**(3), 233-270.

Fenerci, A. and Øiseth, O. (2017), "Measured buffeting response of a long-span suspension bridge compared with numerical predictions based on design wind spectra", *J. Struct. Eng.,* **143**(9). https://doi.org/10.1061/(ASCE)ST.1943-541X.0001873.

Fenerci, A. and Øiseth, O. (2018), "Strong wind characteristics and dynamic response of a long-span suspension bridge during a storm", *J. Wind Eng. Ind. Aerod*., **172**, 116-138. https://doi.org/10.1016/j.jweia.2017.10.030.

Fenerci, A. and Øiseth, O. (2018), "Site-specific data-driven probabilistic wind field modeling for the wind-induced response prediction of cable-supported bridges", *J. Wind Eng. Ind. Aerod*., **181**, 161-179. https://doi.org/10.1016/j.jweia.2018.09.002.

Flay, R. and Stevenson, D. (1988), "Integral length scales in strong winds below 20 m", *J. Wind Eng. Ind. Aerodyn.*, **28**(1-3), 21-30. https://doi.org/10.1016/0167-6105(88)90098-0.

Fujino, Y., Kimura, K. and Tanaka, H. (2012), *Wind Resistant Design of Bridges in Japan: Developments and Practices*, Springer Science & Business Media, Germany.

Grigoriu, M. (1984), "Estimates of extreme winds from short records", *J. StrucT. Eng*. **110**(7), 1467-1484. https://doi.org/10.1061/(ASCE)07339445(1984)110:7(1467).

Gringorten, I.I. (1963), "A plotting rule for extreme probability paper", *J. Geophys. Res.*, **68**(3), 813-814.

Gumbel, E.J. (1954), *Statistical Theory of Extreme Values and Some Practical Applications*, NBS Applied Mathematics Series, National Bureau of Standards, Washington, DC, USA.

Guo, A., Liu, J., Chen, W., Bai, X., Liu, G., Liu, T., Chen, S. and Li, H. (2016), "Experimental study on the dynamic responses of a freestanding bridge tower subjected to coupled actions of wind and wave loads", *J. Wind Eng. Ind. Aerod*., **159**, 36-47. https://doi.org/10.1016/j.jweia.2016.10.003.

Han, Y., Shen, L., Xu, G., Cai, C., Hu, P. and Zhang, J. (2018), "Multiscale simulation of wind field on a long-span bridge site in mountainous area", *J. Wind Eng. Ind. Aerod*., **177**, 260-274. https://doi.org/10.1016/j.jweia.2018.04.012.

Han, Y., Chen, H., Cai, C., Xu, G., Shen, L. and Hu, P. (2016), "Numerical analysis on the difference of drag force coefficients of bridge deck sections between the global force and pressure distribution methods", *J. Wind Eng. Ind. Aerodyn.*, **159**, 65-79. https://doi.org/10.1016/j.jweia.2016.10.004.

He, Y., Chan, P. and Li, Q. (2016), "Observations of vertical wind profiles of tropical cyclones at coastal areas", *J. Wind Eng. Ind. Aerodyn.*, **152**, 1-14. https://doi.org/10.1016/j.jweia.2016.01.009.

Holmes, J.D. (2018), *Wind Loading of Structures*, CRC press, New York, NY, USA.

Hu, P., Han, Y., Xu, G., Li, Y. and Xue, F. (2018), "Numerical simulation of wind fields at the bridge site in mountain-gorge terrain

considering an updated curved boundary transition section", *J. Aerospace Eng*., **31**(3). https://doi.org/10.1061/(ASCE)AS.1943-5525.0000830.

Hu, L., Xu, Y.L. and Huang, W.F. (2013), "Typhoon-induced non-stationary buffeting response of long-span bridges in complex terrain", *Eng. Struct*., **57**, 406-415. https://doi.org/10.1016/j.engstruct.2013.09.044.

Hu, P., Li, Y., Huang, G., Kang, R. and Liao, H. (2015), "The appropriate shape of the boundary transition section for a mountain-gorge terrain model in a wind tunnel test", *Wind Struct., Int. J.*, **20**(1), 15-36. https://doi.org/10.12989/was.2015.20.1.015.

Hu, P., Li, Y., Han, Y., Cai, C. and Xu, G. (2017), "Wind tunnel tests on the characteristics of wind fields over a simplified gorge", *Adv. Struct. Eng.*, **20**(10), 1599-1611. https://doi.org/10.1177/1369433216680635.

Hui, M., Larsen, A. and Xiang, H. (2009), "Wind turbulence characteristics study at the Stonecutters Bridge site: Part II: Wind power spectra, integral length scales and coherences", *J. Wind Eng. Ind. Aerod*., **97**(1), 48-59. https://doi.org/10.1016/j.jweia.2008.11.003.

Kavrakov, I. and Morgenthal, G. (2017), "A comparative assessment of aerodynamic models for buffeting and flutter of long-span bridges", *Engineering*, **3**(6), 823-838. https://doi.org/10.1016/j.eng.2017.11.008.

Larose, G., Zasso, A., Melelli, S. and Casanova, D. (1998), "Field measurements of the wind-induced response of a 254 m high free-standing bridge pylon", *J. Wind Eng. Ind. Aerod*., **74**, 891-902. https://doi.org/10.1016/S0167-6105(98)00081-6.

Li, C., Chen, Z., Zhang, Z. and Cheung, J. (2010), "Wind tunnel modeling of flow over mountainous valley terrain", *Wind Struct*., *Int. J.*, **13**(3), 275-292. https://doi.org/10.12989/was.2010.13.3.275.

Li, Y., Hu, P., Xu, X. and Qiu, J. (2017), "Wind characteristics at bridge site in a deep-cutting gorge by wind tunnel test", *J. Wind Eng. Ind. Aerod*., **160**, 30-46. https://doi.org/10.1016/j.jweia.2016.11.002.

Li, Y.L., Chen, X.Y., Yu, C.J., Togbenou, K., Wang, B. and Zhu, L.D. (2018), "Effects of wind fairing angle on aerodynamic characteristics and dynamic responses of a streamlined trapezoidal box girder", *J. Wind Eng Ind Aerod*., **177**, 69-78. https://doi.org/10.1016/j.jweia.2018.04.006.

Liu, Z., Ishihara, T., Tanaka, T. and He, X. (2016), "LES study of turbulent flow fields over a smooth 3-D hill and a smooth 2-D ridge", *J. Wind Eng. Ind. Aerodyn.*, **153**, 1-12. https://doi.org/10.1016/j.jweia.2016.03.001.

Ma, C., Duan, Q., Li, Q., Liao, H. and Tao, Q. (2019), "Aerodynamic characteristics of a long-span cable-stayed bridge under construction", *Eng. Struct*., **184**, 232-246. https://doi.org/10.1016/j.engstruct.2018.12.097.

Marra, A.M., Mannini, C. and Bartoli, G. (2017), "Wind tunnel modeling for the vortex-induced vibrations of a yawed bridge tower", *J. Bridge Eng.*, **22**(5). https://doi.org/10.1061/(ASCE)BE.1943-5592.0001028.

Masters, F.J., Vickery, P.J., Bacon, P. and Rappaport, E.N. (2010), "Toward objective, standardized intensity estimates from surface wind speed observations", *B. Am. Meteorol. Soc*., **91**(12), 1665-1682. https://doi.org/10.1175/2010BAMS2942.1.

Ren, H., Laima, S., Chen, W.-L., Zhang, B., Guo, A. and Li, H. (2018), "Numerical simulation and prediction of spatial wind field under complex terrain", *J. Wind Eng. Ind. Aerod*., **180**, 49-65. https://doi.org/10.1016/j.jweia.2018.07.012.

Ricciardelli, F. (1996), "Prediction of the response of suspension and cable-stayed bridge towers to wind loading", *J. Wind Eng. Ind. Aerod*., **64**(2-3), 145-159. https://doi.org/10.1016/S0167-6105(96)00088-8.

Rocchi, D., Argentini, T. and Sbrosi, M. (2014), "Pressure distribution and global forces on a bridge deck section: experimental and CFD analysis of static aerodynamic forces", *J. Bridge Eng.*, **20**(9), 04014097. https://doi.org/10.1061/(ASCE)BE.1943-5592.0000695.

Scanlan, R.H. and Tomo, J. (1971), "Air foil and bridge deck flutter derivatives", *J. Soil Mech. Found. Div*., **97**(6), 1717-1737.

Shu, Z., Li, Q., He, Y. and Chan, P. (2017), "Vertical wind profiles for typhoon, monsoon and thunderstorm winds", *J. Wind Eng. Ind. Aerod*., **168**, 190-199. https://doi.org/10.1016/j.jweia.2017.06.004.

Siringoringo, D.M. and Fujino, Y. (2012), "Observed along-wind vibration of a suspension bridge tower", *J. Wind Eng. Ind. Aerodyn.*, **103**, 107-121. https://doi.org/10.1016/j.jweia.2012.03.007.

Tao, T., Wang, H. and Wu, T. (2016), "Comparative study of the wind characteristics of a strong wind event based on stationary and nonstationary models", *J. Struc. Eng*., **143**(5). https://doi.org/10.1061/(ASCE)ST.1943-541X.0001725.

Tse, K., Li, S., Chan, P., Mok, H. and Weerasuriya, A. (2013), "Wind profile observations in tropical cyclone events using wind-profilers and doppler SODARs", *J. Wind Eng. Ind. Aerod*., **115**, 93-103. https://doi.org/10.1016/j.jweia.2013.01.003.

Wang, H., Li, A., Niu, J., Zong, Z. and Li, J. (2013), "Long-term monitoring of wind characteristics at Sutong Bridge site", *J. Wind Eng. Ind. Aerod.*, **115**, 39-47. https://doi.org/10.1016/j.jweia.2013.01.006.

Wu, T. and Kareem, A. (2013), "Bridge aerodynamics and aeroelasticity: A comparison of modeling schemes", *J. Fluids Struct.*, **43**, 347-370. https://doi.org/10.1016/j.jfluidstructs.2013.09.015.

FR